Journal of Membrane Science 732 (2025) 124246

Contents lists available at ScienceDirect

Journal of Membrane Science

journal homepage: www.elsevier.com/locate/memsci

Macroscopic and microscopic gas diffusivity measurements for PIM-COOH/UiO-66-NH_2 composite membranes

Wan-Ni Wu [a,1], Omar Boloki [b,1], Sergey Vasenkov [b], Zachary P. Smith [a,*]

[a] Department of Chemical Engineering, Massachusetts Institute of Technology, 77 Massachusetts Avenue, Cambridge, MA, 02139, USA
[b] Department of Chemical Engineering, University of Florida, Gainesville, FL, 32611, USA

ARTICLE INFO

Keywords:
Pulsed-field gradient NMR
Diffusivity
Gas separation
Mixed-matrix membrane
MOF

ABSTRACT

Mixed-matrix membranes (MMMs) have been heavily studied due to their compelling performance in gas separation applications. Direct measurement of gas diffusivities in MMMs is essential for constructing reliable transport models, but this measurement remains challenging. This study investigates CH_4 and CO_2 diffusion in PIM-COOH and a PIM-COOH/UiO-66-NH_2 MMM with 30 vol% MOF loading, employing ^{13}C pulsed field gradient nuclear magnetic resonance (PFG NMR) and various macroscopic techniques like the time-lag method and sorption analysis. PFG NMR revealed uniform transport properties across pure PIM-COOH films and MMMs on micrometer scales, indicating well-integrated structures without significant defects or MOF clustering. Macroscopically-measured diffusivities derived from the time-lag method showed strong pressure dependence due to the limitations of applying a linear sorption model to microporous materials. In contrast, corrected secant diffusivities aligned closely with self-diffusivities from PFG NMR and exhibited minimal pressure dependence. Application of another common analysis approach, the use of transient sorption experiments, yielded diffusivities with large uncertainties. This comparative study presents the range of diffusivities found by applying various techniques to capture transport and self-diffusivities, highlighting the need to carefully validate model assumptions for diffusion measurements in microporous polymer and MOF-based membrane materials. Of note, this study highlights the strength of PFG NMR in directly probing microscopic transport.

1. Introduction

Mixed-matrix membranes (MMMs), formed by incorporating porous fillers into a polymer matrix, have gained significant attention in gas separation research due to their ability to overcome the inherent limitations of traditional polymeric membranes. Conventional polymeric membranes often struggle with a performance trade-off between selectivity and permeability, a challenge first identified for a large data set by Robeson in 1991 [1]. This challenge has led to extensive research on developing advanced materials such as microporous polymers [2] and MMMs that can surpass the performance upper bound. MMMs, in particular, offer a promising solution by combining the mechanical strength and processability of polymers with the superior separation properties of fillers. Recent advancements have particularly highlighted the use of metal–organic frameworks (MOFs) as fillers [3] due to their tunable pore sizes and versatile chemistry derived from organic linkers, which can be tailored to enhance affinity with certain penetrants or improve compatibility with the polymer matrix. However, a common challenge in MMM fabrication is poor polymer–MOF compatibility, leading to non-selective defects. Various strategies have been proposed to address this challenge, including physically priming the MOF particles with polymers [4–6] and chemically modifying the functional groups of MOF and polymer to enhance their interaction [7].

Understanding the transport properties and the polymer–MOF interface of MMMs is crucial for evaluating and optimizing existing materials, as well as predicting structure–property relationships for new polymer–MOF combinations. Typically, gas diffusion throughout MMMs is quantified using the time-lag method [7,8], back-calculating from permeability and sorption coefficients using the solution–diffusion model [9,10], and/or fitting to transient uptake profiles [11,12]. While these methods provide insights into the transport process through the entire membrane sample, careful experimental design is essential to validate the model assumptions used. Additionally, these experiments can be complicated by factors such as transport barriers at the crystal

* Corresponding author.
E-mail address: zpsmith@mit.edu (Z.P. Smith).
[1] These authors contributed equally.

https://doi.org/10.1016/j.memsci.2025.124246
Received 27 March 2025; Received in revised form 14 May 2025; Accepted 19 May 2025
Available online 20 May 2025

interface and sorption heat-release processes [13]. Therefore, direct measurements of diffusivities are essential to construct accurate transport models and validate existing methodologies.

Pulsed field gradient nuclear magnetic resonance (PFG NMR) has gained traction because it can directly measure microscopic diffusion at relevant length scales within MMMs. Diffusion studies using PFG NMR can quantify diffusion over a broad range of length scales, from hundreds of nanometers to tens of micrometers, which can provide insights into intra- and inter-crystalline self-diffusion. PFG NMR has been instrumental in determining pure- and mixed-component self-diffusivities of light gases and organic solvents in MMMs [14–17]. The localized diffusivity measurement also facilitates assessing the uniformity of transport properties within the MMMs.

In this study, ^{13}C PFG NMR was employed to investigate the microscopic self-diffusion of CH_4 and CO_2 within an MMM composed of carboxylic acid-functionalized PIM-1 (PIM-COOH) and a UiO-66-NH_2 MOF [18]. Previous research has shown that the compatible functional groups on PIM-COOH and UiO-66-NH_2 enhance polymer–MOF interaction, resulting in defect-free MMMs [7]. Pure PIM-COOH films were studied for comparison to understand the role of the MOF on gas transport. Root mean squared displacements (RMSD) of gases were calculated from PFG NMR experiments to elucidate the length scale associated with the self-diffusion process. Additionally, macroscopic diffusion measurements were conducted using the time-lag method, permeation and sorption analyses, and transient sorption experiments. The resulting diffusivities were compared, revealing differences based on various model assumptions, which are carefully discussed as part of this work.

2. Theory related to macroscopic techniques

Transport diffusivities of gas molecules in membranes are measured in the presence of a concentration gradient, and they capture diffusion through the entire sample. Thus, they are also referred to as macroscopically-measured diffusivities. In contrast, self-diffusivity measurements in PFG NMR are performed under equilibrium conditions and typically correspond to a diffusion length scale smaller than the sample size, *e.g.*, smaller than the membrane thickness. Such self-diffusivities are considered microscopic self-diffusivities. Here, we discuss and compare three common methods for obtaining transport diffusivities and how transport diffusivities compare to self-diffusivities obtained from PFG NMR.

2.1. Time-lag method

The time-lag method has been frequently used to obtain gas diffusivities when developing new membrane materials. The time-lag experiment is typically performed using a constant-volume apparatus. A pressure step change is applied to the upstream side of the membrane sample at $t = 0$, and the resulting pressure increase on the downstream side is recorded over time, as illustrated in Scheme 1 (a). The time lag (θ) is determined as the x-intercept of the extrapolated steady-state pressure increase regime. In the simplest form of the time-lag method, the diffusivity (D_θ) is calculated using the following equation [19]:

$$D_\theta = \frac{l^2}{6\theta} \quad \text{Eq 1}$$

where l is the membrane thickness. The advantage of the time-lag method is that one can obtain the permeability (P), D_θ, and the sorption coefficient (S_θ) in one single permeation experiment by applying the solution–diffusion model [20]:

$$P = D_\theta S_\theta \quad \text{Eq 2}$$

While the time-lag method provides a facile approach to obtaining diffusivities with only a small amount of sample, it is based on many assumptions that should be carefully validated. First and foremost, the time-lag method assumes that Henry's law of sorption applies to the membrane material:

$$c = k_D p \quad \text{Eq 3}$$

where c (mmol g^{-1}) is the equilibrium concentration in the sample at pressure p (atm), and k_D is the Henry's sorption coefficient (mmol g^{-1} atm^{-1}). While this assumption is usually true for rubbery polymers, deviation from Henry's law behavior often arises in glassy polymers and microporous materials [21]. A concentration-independent diffusivity is also assumed, which can lead to errors when analyzing the diffusion of species that can interact strongly with the membrane material. Other assumptions regarding the derivation of Eq (1) are listed in Table 1.

Table 1
Key assumptions for using the time-lag method, the secant method, and the transient sorption method to determine gas diffusivities in membranes.

Method	Assumptions
Time-lag method	1. Henry's law sorption ($c = k_D p$) applies 2. Diffusivity is independent of concentration 3. The downstream interface of the membrane is always under vacuum during the permeation test 4. Perfect pressure step-change at the upstream interface at the beginning of the permeation step and no resistance for gas accumulation at the downstream if a constant-volume apparatus is used 5. Fickian diffusion
Secant method	1. Solution–diffusion model applies 2. Fickian diffusion 3. Effective sorption is estimated by the secant slope of the sorption isotherm
Transient sorption	1. Fickian 1D diffusion into an infinite sheet 2. Diffusivity is independent of concentration 3. Instantaneous pressure step-change in the sample chamber at the beginning of the sorption step 4. Chamber pressure does not change significantly due to sorption

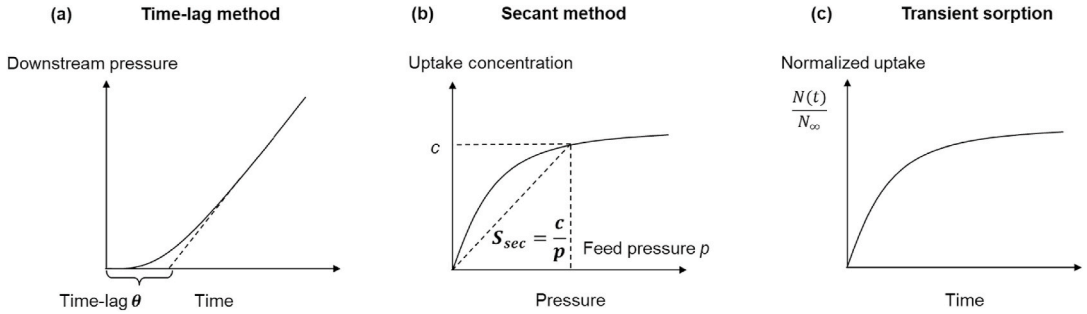

Scheme 1. Key experimental relationships for determining gas diffusivities via (a) the time-lag method, (b) the secant method (permeation and sorption analyses), and (c) the transient sorption profile.

2.2. Secant method (permeation and sorption analyses)

According to the solution–diffusion model, one can also back-calculate the diffusivity by obtaining the permeability from a permeation test and the sorption coefficient from a direct sorption measurement. This method allows one to use the appropriate model that describes the sorption behavior of the sample. The gas sorption isotherms for glassy polymers and microporous materials in composites typically follow the dual-mode sorption (DMS) model (Scheme 1 (b)), in which the concentration of gas sorbed (c) can be calculated as follows [22]:

$$c = k_D p + \frac{C'_H b p}{1 + bp} \quad \text{Eq 4}$$

where a Langmuir mode sorption into the "holes" (excess free volume) of the material is included in addition to the Henry's mode. C'_H is the Langmuir capacity (mmol g^{-1}) and b is the Langmuir affinity constant (atm^{-1}). The DMS parameters obtained from least-square fitting the isotherms are provided in Table S4 for CH_4 and Table S5 for CO_2. Parameters in volumetric units are also included in the tables as they are frequently used for sorption in the membrane field, especially for dual-mode analysis.

The sorption coefficient corresponding to the dual-mode model (S_{sec}) can then be expressed as:

$$S_{sec} = \frac{c}{p} = k_D + \frac{C'_H b}{1 + bp} \quad \text{Eq 5}$$

which has the SI units of mmol m^{-3} Pa^{-1}. The p used for the S_{sec} calculation is the feed pressure of the permeation test. The secant sorption coefficients, in conjunction with the pure-gas permeability, were used to derive the gas diffusivity through membranes using the solution–diffusion model [20]:

$$P = D_{sec} S_{sec} \quad \text{Eq 6}$$

where D_{sec} is the gas diffusivity derived from this method. Key assumptions of this method are listed in Table 1.

2.2.1. Solution–diffusion model with partial immobilization

The solution–diffusion model with partial immobilization assigns different diffusivities to the molecules sorbed as the Henry's and Langmuir modes. The permeability is expressed as:

$$P = D_D k_D + D_H \frac{C'_H b}{1 + bp}, \quad \text{Eq 7}$$

where D_D is the diffusivity corresponding to the Henry's mode population and D_H is the diffusivity of the molecules sorbed onto the Langmuir modes [23–25]. Both D_D and D_H are assumed to be constant. The parameter $F = D_H/D_D$ is often used to describe the ratio of the diffusivities of these two modes. D_D is assumed to be greater than D_H, thus $0 \le F \le 1$. $F = 0$ is the limiting case where the Langmuir sites are completely immobile. The F parameter can be obtained by measuring the permeability as a function of the feed pressure and fitting the data to **Eq 8.** [23]

$$P = k_D D_D \left[1 + \frac{F}{1 + bp} \frac{C'_H b}{k_D}\right] \quad \text{Eq 8}$$

2.3. Transient sorption

The gas uptake of a sample over time (Scheme 1 (c)) can also be used to derive gas diffusivities. Transient gas uptake experiments are typically performed using a constant volume apparatus based on a pressure decay method or a gravimetric uptake experiment [11,12,26]. Here, the pressure decay method is adopted. The moles of gas sorbed into the sample over time, $N(t)$, correspond to the decay in the chamber pressure, $P(t)$:

$$\frac{N_k(t) - N_{\infty,k-1}}{N_{\infty,k} - N_{\infty,k-1}} = \frac{P(t) - P_{0,k}}{P_{\infty,k} - P_{0,k}} \quad \text{Eq 9}$$

where $P_{0,k}$ and $P_{\infty,k}$ are the pressures of the chamber at the beginning and the end of step k. The pressure decay profile can be fitted to the solution to a problem with 1D diffusion into an infinite sheet:

$$\frac{\partial C}{\partial t} = D_{ts} \frac{\partial^2 C}{\partial x^2} \quad \text{Eq 10}$$

where C is the concentration of gas in the membrane, D_{ts} is the diffusivity associated with the transient sorption process, which is assumed to be independent of concentration, t is the total exposure time, and x is the direction along the thickness of the membrane. The initial conditions are:

$$N_k(t) = 2\int_0^h C(t)dx, \text{ and } \quad \frac{N_k(t) - N_{\infty,k-1}}{N_{\infty,k} - N_{\infty,k-1}} = 0 \quad \text{Eq 11}$$

where $N_k(t)$ is the total amount of gas in the membrane at time t during the pressure step k, $N_{\infty,k}$ is the total amount of gas in the membrane at equilibrium for pressure step k, and h is half the thickness of the membrane (*i.e.* $h = l/2$). The boundary conditions are:

$$C \cong C_1 \quad \text{at} \quad x = \pm h, \quad \text{Eq 12}$$

$$\frac{\partial C}{\partial x} = 0 \quad \text{at} \quad x = 0 \quad \text{Eq 13}$$

where C_1 is the gas concentration at the membrane surface, which is assumed to be constant. This assumption holds for the pressure ranges relevant to the permeation tests in this study, as gas sorption into the membrane resulted in less than a 2.5 % decrease in the chamber pressure. However, it is important to note that this assumption becomes increasingly inaccurate at lower pressures. For instance, when the chamber pressure is below 1 atm, membrane sorption can lead to a pressure reduction of up to ~40 %.

The analytical solution to the diffusion problem is [12,27]:

$$\frac{N_k(t) - N_{\infty,k-1}}{N_{\infty,k} - N_{\infty,k-1}} = 1 - \frac{8}{\pi^2} \sum_{n=0}^{\infty} \frac{1}{(2n+1)^2} \exp\left[-D_{ts}\left(n + \frac{1}{2}\right)^2 \pi^2 t \Big/ h^2\right] \quad \text{Eq 14}$$

We can recover the gas diffusivity by fitting the pressure decay profile in Eq (9) obtained experimentally to Eq (14). Since the derived diffusivity scales with the square of film thickness, small variations in the sample thickness can lead to significant errors. Key assumptions of this method are listed in Table 1.

2.4. Corrected diffusivities

To allow for comparison to the self-diffusivities obtained from PFG NMR measurements, the transport diffusivities were converted to corrected diffusivities (or Maxwell–Stefan diffusivities) (D_{corr}) via the Darken-type relationship [28–30]:

$$D_T = D_{corr} \left(\frac{\partial \ln p}{\partial \ln c}\right)_{Temp} \quad \text{Eq 15}$$

where p is the pressure of the bulk gas that is in equilibrium with the adsorbed phase at concentration c. D_T is the transport diffusivity, which can be D_θ, D_{sec}, or D_{ts}. Since a concentration gradient from the feed pressure to vacuum exists within the membrane during a permeation test, the thermodynamic factor $\left(\frac{\partial \ln p}{\partial \ln c}\right)_{Temp}$ was taken at the pressure that is half of the feed pressure as an estimate of the average thermodynamic

factor in the membrane when correcting D_θ and D_{sec}. The thermodynamic factor was evaluated at the final equilibrium pressure when correcting D_{ts}, since the gradient in the sample during the sorption measurement is smaller.

3. Materials and methods

3.1. Materials

Methanol (HPLC, ≥99.9 %), N, N-dimethylformamide (anhydrous DMF, 99.8 %), chloroform (stabilized with 100–200 ppm amylene, ≥99.5 %), tetrahydrofuran (THF, ACS Reagent Grade, ≥99.0 %, stabilized with 250 ppm butylated hydroxytoluene), glacial acetic acid (Ph Eur grade), and sulfuric acid (95.0–98.0 %) were purchased from Sigma-Aldrich and used as received. 2-Aminoterephthalic acid (BDC-NH_2, 99 %) was purchased from Fisher Scientific and stored in a desiccator under vacuum prior to use. Zirconium chloride ($ZrCl_4$, sublimed grade, 99.95 %) was purchased from Strem and stored in a desiccator under static vacuum prior to use. Ultrahigh purity CH_4 (99.97 %) and CO_2 (99.99 %) were purchased from Linde for gas transport testing. PIM-COOH was hydrolyzed from a PIM-1 polymer synthesized in-house following reported procedures [7]. The monomers for PIM-1, 5,5′,6,6′- tetrahydroxy-3,3,3′,3′-tetramethyl-1,1′-spirobisindane (TTSBI, 96 %) and 1, 4-dicyanotetrafluorobenzene (DCTB, 99 %), were obtained from Sigma-Aldrich and were stored in a desiccator under static vacuum prior to use.

UiO-66-NH_2 nanoparticles were synthesized using an acetic acid-modulated solvothermal synthesis following established procedures [7]. A MOF particle size of 130 ± 20 nm was found from transmission electron microscopy (TEM) imaging (Fig. S1), and a BET surface area of 1400 ± 100 m^2/g was obtained from N_2 adsorption analysis (Fig. S2). PIM-1 was synthesized in-house and converted into PIM-COOH through an acid hydrolysis reaction in a suspension state, as previously reported [7]. The conversion of nitrile groups to carboxyl groups was determined to be 82 % via thermogravimetric analysis (TGA), as shown in Fig. S3.

3.2. Membrane casting

PIM-COOH and approximately 30 vol% PIM-COOH/UiO-66-NH_2 mixed-matrix membranes (MMMs) were fabricated using an evaporative casting method. Pure polymer films were prepared by dissolving 200 mg of PIM-COOH in 2 mL of THF. The polymer solutions were filtered (Whatman™ Puradisc™ PTFE filter, 5 μm) and cast into glass petri dishes (STERIPLAN® Petri Dishes, 60 mm × 15 mm) on a leveled platform within a THF vapor-saturated glove bag.

The MMMs were prepared by first dissolving 200 mg of PIM-COOH in 0.75 mL of THF to create a highly viscous polymer solution. The polymer solution was left to homogenize on a roller overnight. Then, the appropriate amount of MOF suspension in THF was added to the polymer solution to obtain a MOF loading of approximately 30 wt% of the polymer. The polymer–MOF mixture was probe-sonicated for 30 s and allowed to homogenize on a roller overnight. Finally, the mixture was probe-sonicated once more, filtered through a Kimwipe-packed glass pipette to remove any MOF aggregates, and immediately cast into glass petri dishes on a leveled platform inside a THF vapor-saturated glove bag. This filtering step often resulted in a lower MOF loading than the targeted 30 wt%.

All casting solutions were left to evaporate in a glove bag for approximately 48 h, followed by further drying at 130 °C under vacuum for 12 h. The prepared films were subsequently used for pure-gas sorption, PFG NMR, and pure-gas permeation measurements.

3.3. Characterization

3.3.1. Microscopy

The morphology and estimated size of the MOF nanoparticles were assessed with an FEI Tecnai transmission electron microscope (TEM). TEM samples were prepared on TEM grids (Electron Microscopy Sciences, Formvar, 400 mesh, copper, FF400-CU-TH). A sample of MOF suspended in methanol was taken and applied to the grid using a pipette.

3.3.2. MOF N_2 adsorption at 77 K

The Brunauer−Emmett−Teller (BET) surface area of UiO-66-NH_2 MOF powders was measured using N_2 adsorption isotherms at 77 K on a Micromeritics 3Flex system. BET surface area of the UiO-66-NH_2 samples was calculated in compliance with BET fitting criteria. For detailed information on BET analysis, readers can refer to references. [31–34] Approximately 100 mg of MOF was placed in a sample tube and degassed at 100 °C for 12 h. The UiO-66-NH_2 used for membrane fabrication showed a BET surface area of 1400 ± 100 $m^2\ g^{-1}$ and a cumulative pore volume (v_{pore}) of 0.63 $cm^3\ g^{-1}$ for pores up to 20 Å, as calculated using density functional theory (DFT). Given the MOF pore volume and the skeletal density (ρ_{sk}) of 1.9 g cm^{-3} reported previously [7], the apparent density of UiO-66-NH_2 was calculated as:

$$\rho_{app} = \frac{\rho_{sk}}{(\rho_{sk} v_{pore}) + 1} = 0.86\ \text{g cm}^{-3}. \quad \text{Eq 16}$$

3.3.3. MMM loading

The weight loading of MOF in MMMs was obtained by thermogravimetric analysis (TGA) in air (TA Instruments Thermogravimetric Analyzer 550). Approximately 10 mg of sample was held at 100 °C for 30 min in N_2 to remove any absorbed moisture and subsequently ramped to 800 °C at a rate of 10 °C min^{-1} under air. The TGA data was normalized to 100 wt% at 100 °C. The weight loadings (wt%) of the MMMs were calculated according to the following equations:

$$M_{MOF} = \frac{M_{pol}(\%_{MMM} - \%_{polymer})}{\%_{MOF} - \%_{MMM}} \quad \text{Eq 17}$$

$$wt\% = \frac{M_{MOF}}{M_{MOF} + M_{pol}} \quad \text{Eq 18}$$

where M_{pol} is the mass of PIM-COOH (g) in the MMM, M_{MOF} is the mass of MOF (g) in the MMM, and $\%_{polymer}$, $\%_{MOF}$, and $\%_{MMM}$ are the remaining percentages of PIM-COOH, UiO-66-NH_2, and MMM from the TGA curve at 800 °C. The density of UiO-66-NH_2 reported in Eq Eq (16) and a PIM-COOH density of 1.23 ± 0.01 g cm^{-3} were used to convert the MOF wt% to vol%. The density measurement for PIM-COOH was performed in hexadecane at 23 °C using a Mettler Toledo density kit based on Archimedes' principle.

3.3.4. Pure-gas sorption

CH_4 and CO_2 sorption experiments were performed for PIM-COOH films, UiO-66-NH_2 powders, and MMMs at 35, 50, and 65 °C using an automated constant-volume system from Maxwell Robotics with a pressure decay method. In a typical test, around 120–150 mg of samples were loaded into the sample cell, which was then sealed with a VCR gasket. The system was initially degassed for 10 h to remove any sorbed gases and for 1 h between each temperature or gas switch. The amounts of gas sorbed into the sample at each pressure step were calculated using a mole balance between the initial and final pressures in the chamber. The gas fugacity was estimated from pressure using the virial equation of state truncated to include terms up to the third virial coefficient.

The isotherms collected for the pure-polymer and MMM films were fitted to the DMS model (Eq (4)). The isotherms collected for UiO-66-NH_2 were fitted to the single-site Langmuir–Freundlich equation [35, 36]:

$$\frac{Q}{Q_m} = \frac{B \times p^{1/t}}{1 + B \times p^{1/t}} \quad \text{Eq 19}$$

where Q_m is the saturation uptake at equilibrium (mmol g^{-1}), Q is the adsorption amount in the experiment (mmol g^{-1}), p is the equilibrium pressure (atm), and t and B are the Freundlich and Langmuir parameters, respectively. The Langmuir–Freundlich model was chosen for the MOF material because gas sorption in pure MOF samples occurs primarily via adsorption onto saturable sorption sites, a behavior well described by the Langmuir isotherm. The Freundlich component accounts for the surface heterogeneity introduced by amine functionalization by allowing a range of adsorption energies. Combining these features, the Langmuir–Freundlich model provides a more accurate and physically representative fit to the pure MOF sorption isotherms. The fitted parameters are shown in Table S6.

3.3.5. Isosteric heat of sorption

The isosteric heats of sorption (Q_{st}) were calculated from the fitted isotherms for PIM-COOH, 30 vol% MMM, and UiO-66-NH_2 using the Clausius–Clapeyron equation:

$$\frac{d\ln P}{d(1/T)} = -\frac{Q_{st}}{R} \quad \text{Eq 20}$$

The values are plotted against the gas uptake in the samples in Fig. S4.

3.3.6. Transient sorption

The pressure decay profile in each pressure step during the sorption test was also used to derive gas diffusivities in the film samples. The derivation is shown in Eq (9) to Eq (14). The uncertainties of the diffusivities were calculated using error propagation, which includes the standard error of the fit and a 30 % relative error in the sample thickness.

3.3.7. Pure-gas permeation

CH_4 and CO_2 pure-gas permeation tests were performed on PIM-COOH films and the MMMs at 35, 50, and 65 °C using automated constant-volume, variable-pressure systems, as detailed in previous work [8,37–39]. The films for these tests were aged for two months to minimize the effects of aging, which is typically most significant in the first two weeks after casting [40,41]. For testing, the films were glued onto brass disks using Devcon 5-min epoxy. Samples from different films were tested in triplicate, with the standard deviation of the triplicates reported as error bars. While the CO_2 feed pressures used in this study were below the plasticization pressure found at 35 °C for PIM-COOH previously [7], a different piece of PIM-COOH was cut out from the film for CO_2 permeation to eliminate any potential effects of plasticization. PIM-COOH/UiO-66-NH_2 MMMs show strong resistance to CO_2-induced plasticization up to 40 atm [7], thus the MMM samples were all tested for the full sequence of gas and temperature steps.

In a typical permeation test, the system was degassed for 6 h initially and for 1 h between steps. Once residual gas from the previous step was removed, the membrane was exposed to the feed gas at the upstream side, and the pressure increase from vacuum on the downstream side was recorded. The pure-gas permeability was then calculated from the steady-state increase in downstream pressure:

$$P = \frac{lV_d}{(p_2 - p_1)ART} \times \left[\left(\frac{dp_1}{dt}\right)_{SS} - \left(\frac{dp_1}{dt}\right)_{leak}\right] \quad \text{Eq 21}$$

where P is the permeability in barrer (10^{-10} cm^3(STP) cm cm^{-2} $cmHg^{-1}$ s^{-1}), l is the thickness of the membrane (cm), V_d is the downstream volume (cm^3), A is the exposed membrane area (cm^2), R is the gas constant (0.278 cmHg cm^3 cm^{-3} K^{-1}), T is the absolute temperature (K), p_1 is the downstream pressure (cmHg), p_2 is the upstream pressure (cmHg), $\left(\frac{dp_1}{dt}\right)_{ss}$ is the steady-state downstream pressure (cmHg s^{-1}), and $\left(\frac{dp_1}{dt}\right)_{leak}$ is the leak rate (cmHg s^{-1}). Pure-gas diffusivities were determined via the time-lag method using Eq (1). The permselectivity is the ratio of the CO_2 and CH_4 permeabilities, and can also be decoupled into diffusivity selectivity and sorption selectivity:

$$\alpha_{CO_2/CH_4} = \frac{P_{CO_2}}{P_{CH_4}} = \left(\frac{D_{CO_2}}{D_{CH_4}}\right)\left(\frac{S_{CO_2}}{S_{CH_4}}\right) \quad \text{Eq 22}$$

The permeation feed pressure was selected to match the pressure used for the PFG NMR tests. The feed pressure for each test is provided in Table S1. To understand the dependence of gas diffusivities on the feed pressure, a PIM-COOH sample and a 30 vol% MMM sample were exposed to 1× , 2× , and 3× of the feed pressures listed in Table S1.

3.4. PFG NMR sample preparation

The samples for PFG NMR studies were prepared by placing membrane strips of around 15–25 mm in length and 2–3 mm in width of a selected membrane film into a 5 mm medium wall NMR tube (Wilmad Labglass, Inc). Approximately 80–100 mg of such strips were placed into the tube for each PFG NMR experiment. The tube was then attached to a custom-made vacuum system, where the sample was degassed under high vacuum for 8 h at 100 °C. After the activation step, the sample was cooled down gradually to 25 °C. ^{13}C-labeled CO_2 and CH_4 with 99 % isotopic purity (Sigma-Aldrich) were used as sorbates. Sorbate loading was performed by cryogenically condensing the desired mass of a single component gas into the NMR tube using liquid nitrogen. After loading, the sample was flame-sealed and separated from the vacuum system. The sample was then stored for at least 12 h at 25 °C. Before performing any NMR experiments, the sample was kept in the spectrometer at the desired measurement temperature (35, 50, or 65 °C) for at least 1 h to ensure that the sorption equilibrium at this temperature was established. Selected NMR experiments were performed immediately after the equilibration and then repeated several hours later to confirm that the equilibration time was sufficiently long. The observation of reproducible NMR data enabled confirmation of sorption equilibrium following the chosen equilibration time.

The intra-membrane concentrations and loading pressures were determined using NMR spectroscopy (Table S2 and S3) following the procedure discussed in the literature [14,42,43]. The NMR pressure conditions were chosen to maintain similar gas loadings in the MMM or PIM-COOH samples across the three temperatures and to ensure that both PIM-COOH and the MMM were under the same pressure for the same gas at 35 °C. The intra-membrane sorbate concentrations and bulk gas densities in the studied samples were quantified by utilizing the proportionality between the area under the NMR spectrum and the number of sorbate molecules in the measured part of the samples. To establish the proportionality constants between the area under the NMR spectrum and the amount of sorbate, reference samples containing only bulk gases at known bulk gas densities were measured. The total NMR signal obtained from the membrane samples included contributions from both the intra-membrane region and the surrounding bulk gas phase. These contributions were quantified separately using a mass balance approach with the following known properties: (i) total mass of gas loaded in the NMR tube (ii) volume of the sealed NMR tube, (iii) the total volume of the membrane pieces used and the total volume of the bulk gas phase in the active range of the NMR radiofrequency coil [14]. Using this approach, the gas density in the bulk gas phase of each sample was determined, and this gas density was then used to determine gas pressure at the measurement temperature by applying a known equation of state [44,45].

3.5. PFG NMR measurements

^{13}C PFG NMR diffusion measurements were performed using a 14 T Avance III spectrometer (Bruker Biospin) operating at a ^{13}C frequency of 149.8 MHz and a ^{1}H frequency of 600 MHz. The magnetic field gradients

with amplitudes up to 17 T m^{-1} were generated using a *DiffBB* diffusion probe. Most of the measurements were performed using ^{13}C PFG NMR. The benefit of using ^{13}C PFG NMR rather than the traditional ^{1}H PFG NMR is to take advantage of longer T_2 NMR relaxation times for ^{13}C than for ^{1}H for gases in the membranes. However, selected experiments for samples loaded with CH_4 were also performed using ^{1}H PFG NMR to ensure the reliability and consistency of the data. No differences, within uncertainty, were observed between the data measured using the two nuclei, confirming the absence of any measurement artifacts.

Bipolar, sinusoidal, and trapezoidal shaped gradient pulses with effective durations between 1 and 2.5 ms were used. It is important to note that the gradient pulse duration and shape were the same for all the measurements of any sample. Sinusoidal shaped pulses were primarily used. However, to achieve a larger area under a gradient pulse, trapezoidal shaped pulses were utilized for the samples exhibiting slower self-diffusion to achieve sufficiently large PFG NMR signal attenuations. The effective gradient strength used ranged between 0.03 and 17 T m^{-1}. The effective diffusion time used ranged between 10 and 640 ms for both sorbates and membrane types. A longitudinal eddy current delay of 6 ms was used. The total duration of a single ^{13}C PFG NMR diffusion experiment varied from around 1–3 h with a total number of scans between 64 and 144. The repetition delays varied between 2 and 4 s to be at least 1.5 times larger than the corresponding T_1 NMR relaxation time.

The diffusion experiments were conducted using the 13-interval pulse sequence [46] exhibiting bipolar gradients and an additional longitudinal eddy current delay [47]. This sequence was used to minimize or eliminate inhomogeneities in the magnetic field (*i.e.,* magnetic susceptibility effects). These inhomogeneities are expected for heterogeneous systems such as stacked film pieces used in this work. The measured PFG NMR attenuation curves, which are dependencies of the normalized PFG NMR signal intensity on the effective magnetic field gradient strength (g), were used to obtain self-diffusion coefficients (D_{NMR}). In the case of normal self-diffusion with a single self-diffusion coefficient (D_{NMR}), the PFG NMR attenuation curves can be described using the following equation [48]:

$$\psi = \frac{S(g)}{S(g \sim 0)} = \exp\left(- q^2 D_{NMR} t_{eff} \right) \quad \text{Eq 23}$$

where ψ is the PFG NMR signal attenuation, S is the PFG NMR signal at gradient strength g, and t_{eff} is the effective diffusion time (*i.e.*, the diffusion observation time) [46]. The parameter q is given by $q = 2\gamma\delta g$, where γ, is the gyromagnetic ratio, and δ is the effective duration of one gradient pulse. For three-dimensional diffusion, the RMSD can be related to the self-diffusivity using the Einstein relation [48]:

$$\langle r^2 \rangle^{1/2} = \sqrt{6 D_{NMR} t_{eff}} \quad \text{Eq 24}$$

The experimental error was assessed by considering the following factors: (i) the reproducibility of the data from measurements of two identically prepared but distinct samples under the same experimental conditions and (ii) the reproducibility of the data when measurements of the same sample were performed using different nuclei (^{13}C or ^{1}H) for CH_4 samples.

Longitudinal (T_1) and transverse (T_2) NMR relaxation times of CO_2 and CH_4 were measured using the standard inversion recovery and standard Carr-Purcell-Meiboom-Gill (CPMG) pulse sequences, respectively. The tau value used in the CPMG pulse sequence was 100 μs. For all studied samples, the NMR relaxation data were consistent with no distribution over relaxation times for both T_1 and T_2 relaxation. The T_1 ^{13}C NMR relaxation time was observed to be in the range of 0.8–1.6 s for the MMM and the PIM-COOH samples. The T_2 ^{13}C NMR relaxation times were in the range between 9 and 97 ms. All NMR relaxation data are presented in Tables S10 and S11.

4. Results and discussion

4.1. Equilibrium sorption analysis

The sorption isotherms of CH_4 and CO_2 in PIM-COOH films, MMMs, and pure MOF particles at 35, 50, and 65 °C are shown in Fig. 1. The pure MOF sample exhibited the highest gas uptake as expected due to its high BET surface area and porosity. A prediction of the gas uptake in a 30 vol% MMM at 35 °C was made based on an additivity assumption—namely, that the total uptake is the weighted sum of the individual uptakes from the MOF and polymer phases. The predicted curve aligned remarkably well with the actual measurement, indicating that there was no noticeable pore obstruction from polymer infiltrating the porous network.

The isosteric heats of sorption (Q_{st}) were calculated from the isotherms, with values plotted in Fig. S4. While UiO-66-NH_2 had a similar Q_{st} for CH_4 as PIM-COOH, it showed a higher Q_{st} for CO_2 due to its strong CO_2 affinity from the amine groups [49]. Consequently, incorporating MOF into PIM-COOH resulted in a slightly higher Q_{st} for the MMM as compared to PIM-COOH alone within the CO_2 concentration range of interest (1.11–1.56 mmol g^{-1}), which was considered for subsequent PFG NMR and permeation tests.

4.2. PFG NMR

The PFG NMR attenuation curves presented in Fig. 2 and Fig. S5 for CO_2 and CH_4, respectively, exhibit a mono-exponential behavior, appearing linear in the semi-logarithmic representation. The attenuation curves also show no dependence on the diffusion time for the range of diffusion times used. This finding aligns with Eq (23), as shown by the average fitted lines in these figures, thus providing evidence for a single self-diffusivity that is independent of diffusion time for each sample, temperature, and gas measured. The PFG NMR signal from the bulk gas molecules diffusing outside the membrane was attenuated at the smallest gradient strength applied, effectively eliminating any contribution from bulk gas molecules to the measured signal. The self-diffusivities of CO_2 and CH_4 were measured by PFG NMR in reference NMR samples containing only a single-component bulk gas at the pressure and temperature similar to those used for membrane NMR samples (Table S16). It was observed that the bulk gas self-diffusivities were at least 5 orders of magnitude larger than the corresponding gas self-diffusivities measured inside the membranes.

The intramembrane self-diffusivities from the best fit of the attenuation curves using Eq (23) and the corresponding RMSDs, calculated using Eq (24), are presented in Tables S12 and S13. The smallest RMSDs (1.0 μm) measured for the MMM were much larger than the average size of the UiO-66-NH_2 crystals (0.13 μm). Hence, the reported self-diffusivities for the MMMs correspond to the diffusion of gases under fast exchange conditions between molecules diffusing in UiO-66-NH_2 and PIM-COOH. The lack of deviations of the PFG NMR attenuation curves from the mono-exponential behavior as well as their independence of the effective diffusion time and the corresponding RMSDs suggest that the membrane transport properties are uniform across all length scales considered. The independence of D_{NMR} on the diffusion time also implies that the residence time of gas molecules in a single MOF crystal is much shorter than the smallest diffusion time used in PFG NMR, which was 10 ms. Gas self-diffusivities measured at the same temperature are higher in the MMM than in the pure PIM-COOH polymer for both gases due to the faster diffusion in the MOF phase of the MMM compared to the polymer phase.

4.3. Pure-gas permeation

CH_4 and CO_2 pure-gas permeation tests were conducted at feed pressures that matched the pressures used in the PFG NMR tests, as detailed in Table S1. Fig. 3 (a) shows the CO_2/CH_4 selectivity plotted

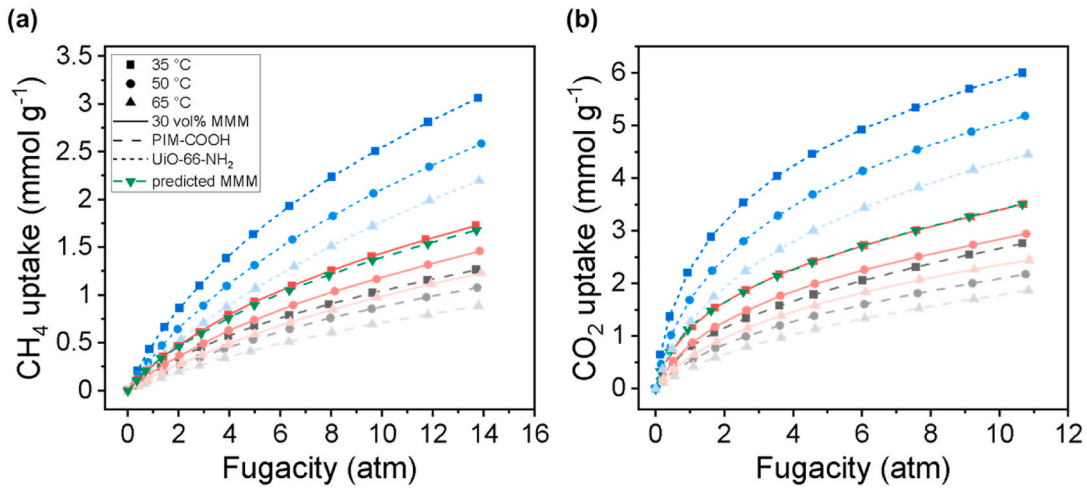

Fig. 1. (a) CH_4 and (b) CO_2 sorption isotherms for PIM-COOH films, 30 vol% MMMs, and UiO-66-NH_2 powders at 35, 50, and 65 °C. The blue, red, and gray curves are for UiO-66-NH_2, MMM, and PIM-COOH, respectively. The green curve represents the predicted uptake for a 30 vol% (23 wt%) MMM at 35 °C using an additive model to combine polymer and MOF uptake values. (For interpretation of the references to colour in this figure legend, the reader is referred to the Web version of this article.)

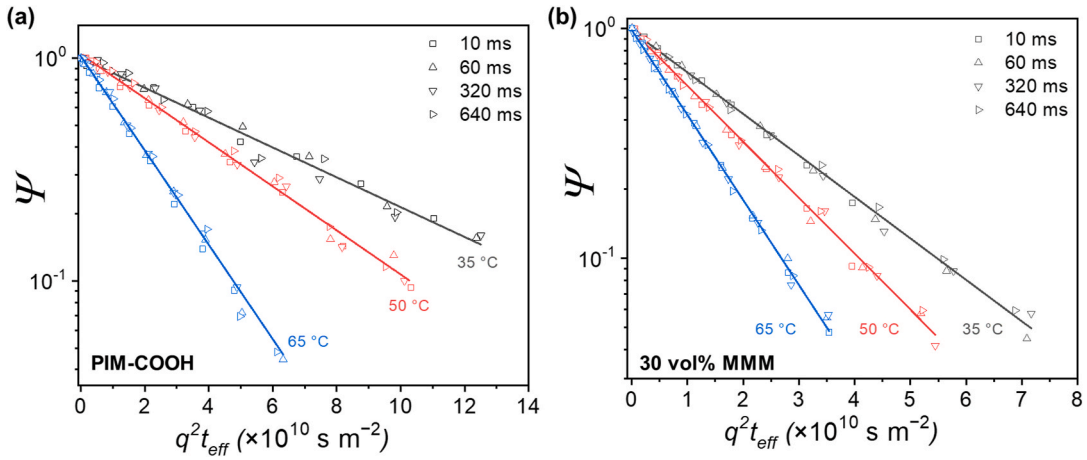

Fig. 2. ^{13}C PFG NMR attenuation curves measured for (a) PIM-COOH films and (b) 30 vol% MMMs loaded with CO_2 at 35, 50, and 65 °C. The solid lines represent the fitting results to Eq (23).

against the CO_2 permeability, along with the 2008 pure-gas upper bound for CO_2/CH_4. Fig. 3 (b) decouples the selectivity into its diffusion and sorption contributions using D_{sec} and S_{sec}. In terms of permeability and permselectivity, the MMM demonstrated higher permeability compared to PIM-COOH, placing its performance at 35 °C on the upper bound, consistent with previously reported results [7]. It is important to note that the data used to determine the upper bound were mostly collected at 35 °C, and the CO_2/CH_4 upper bound is expected to shift downwards at elevated temperatures [50].

The similar selectivity for PIM-COOH and the MMM can be attributed to the large pore aperture of UiO-66-NH_2 (~6 Å) compared to the kinetic diameters of CO_2 (3.3 Å) and CH_4 (3.8 Å) [51], providing minimal size-sieving advantages with the MOF. This result is evident in Fig. 3 (b), where the diffusion selectivities for PIM-COOH and the MMM are within statistical error. Although the addition of amine-functionalized MOF was anticipated to increase the CO_2 affinity of the MMM, the MOF addition only showed a slight increase in the sorption selectivity.

As the temperature increased, the permeability for both samples remained relatively constant. This finding is due to the opposing effects of diffusivity, which increases with temperature, and sorption, which decreases with temperature. However, the overall selectivity decreased with increasing temperature, which was caused by both diffusion and sorption selectivity decreasing (Fig. 3 (b)). This decrease in selectivity is expected, as the CO_2 selectivity over CH_4 is driven by the smaller molecular size and the higher solubility of CO_2. Since both diffusion and sorption are activated processes, the increase in temperature lowers both selectivities [50].

Fig. 3 (c) shows the time-lag and secant diffusivities, while Fig. 3 (d) shows the corresponding sorption coefficients. The incorporation of the highly porous MOF increased both the diffusivities and sorption coefficients for CH_4 and CO_2 compared to PIM-COOH, resulting in higher permeability. This trend was consistent across the investigated temperature range. When comparing the diffusivities obtained from the two methods for the same sample, D_θ was consistently lower than D_{sec}. This discrepancy arises from assumptions in the time-lag method, which may not be appropriate to apply to microporous materials. Eq (1) is strictly valid only for systems with Henry's sorption behavior (which is usually not a reasonable model to apply to glassy polymers like PIM-COOH) and for systems with a diffusivity that is independent of concentration [19]. Therefore, while the time-lag method provides a simple way to estimate diffusivities for comparison, the values are often inaccurate when applied to glassy and microporous materials [11]. Lanč et al. demonstrated that the linear concentration profile assumed by the time-lag

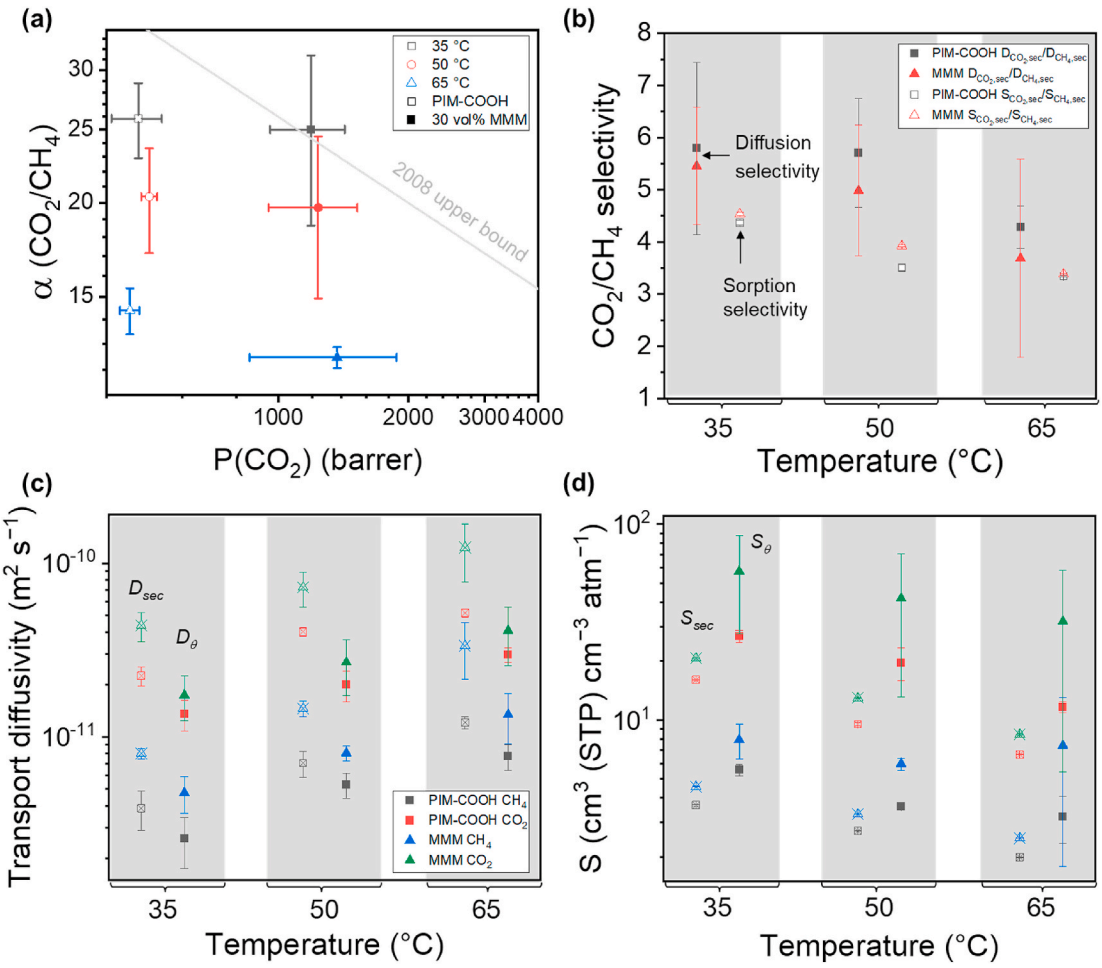

Fig. 3. (a) CO_2/CH_4 upper bound plot for PIM-COOH and 30 vol% MMMs tested at 35, 50, and 65 °C under pure-gas feed pressures listed in Table S1. Note that the upper bound was derived from data collected around 35 °C [50,52]. (b) CO_2/CH_4 diffusion and sorption selectivity derived from the secant method. Time-lag and secant (c) diffusivities and (d) sorption coefficients of CH_4 and CO_2. The data points in each gray box were collected under the same temperature.

method underestimates the concentration in the membrane. Given the concave shape of the sorption isotherms, an underestimated concentration leads to an overestimated sorption coefficient, resulting in systematically lower D_θ values. The time lag is also dependent on sample history, such as the degas time before the permeation run and the duration of the experiment [25]. Since sorption tests are performed at equilibrium, they are less influenced by sample history and generally provide more reproducible transport properties compared to the time-lag method [11].

4.4. Transient sorption

Diffusivities were also obtained through transient sorption experiments using the same apparatus as the equilibrium sorption test, denoted as D_{ts}. The pressure decay profile at the beginning of each pressure step in the sorption sequence was extracted and fitted to Eq (14) to determine the diffusivity. All the diffusivities obtained in this study are plotted in Fig. 4 for comparison. Among the methods for measuring transport diffusivities, the transient sorption method yielded the lowest values, sometimes less than 30 % of the corresponding D_{sec}. Similar findings were reported by Lanč et al., who attributed the low D_{ts} values to the transient sorption experiments primarily capturing the Langmuir behavior rather than Henry's sorption [11]. For glassy polymers, the diffusion associated with the Henry's law mode (D_D) is significantly higher than that in the Langmuir mode (D_H) [21], leading to a substantial underestimation of diffusivity in transient sorption experiments. The ratio of D_H to D_D was estimated by performing variable pressure permeation tests, and the values were less than 0.3 for both PIM-COOH and MMMs at all temperatures (Table S9). This finding confirmed that the reasoning provided by Lanč et al. for the low D_{ts} is also applicable to our system. High uncertainties are also found for D_{ts}, with notable sources of error from both the large pressure fluctuation in the transient regime (Fig. S6), which can hinder an accurate fit representative of the actual pressure decay [12], and the variation in sample thickness.

When comparing the macroscopically-measured diffusivities to the self-diffusivities, the transport diffusivities were corrected using Darken's relationship (Eq (15)) to account for nonidealities in the system. Self-diffusivity is not directly related to the flow conditions used in membrane applications. Instead, it quantifies the intrinsic rate of molecular diffusion under equilibrium conditions, where the sorbate concentration is uniform throughout the membrane and thermodynamic driving forces are absent. In contrast, transport diffusivities measured by macroscopic techniques represent effective or average values, as they are typically affected by non-uniform sorbate concentration profiles within the membrane during operation. This concentration dependence of transport diffusivity can occur even in the absence of plasticization, due to factors such as sorption site saturation and polymer–sorbate interactions [53].

For process-scale transport modeling and unit operation simulations, transport diffusivities are generally more relevant, as they capture the separation process dynamics. Conversely, self-diffusivity measurements and analysis of the associated diffusion regime provide valuable insights

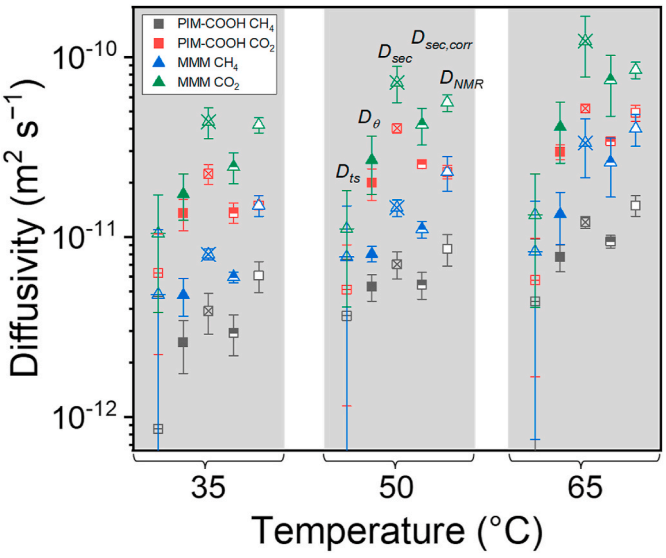

Fig. 4. Diffusivities of CH_4 and CO_2 in PIM-COOH and a 30 vol% MMM obtained from transient sorption experiments (D_{ts}), the time-lag method (D_θ), the secant method with ($D_{sec,corr}$) and without (D_{sec}) thermodynamic correction, and PFG NMR measurements (D_{NMR}). The data points within a gray box were collected at the same temperature. The error bars for D_{ts} were calculated from error propagation, and the error bars for D_θ, D_{sec}, $D_{sec,corr}$, and D_{NMR} were calculated from testing replicates.

into the fundamental transport properties of the membrane material itself. In cases where the concentration dependence of transport diffusivity is negligible, self-diffusivities are expected to approach the corrected diffusivities.

Here, D_{sec} were considered the most reliable diffusivities as they showed low uncertainties, and the secant method did not include unrealistic assumptions for glassy polymers. Therefore, Darken's correction was applied to D_{sec} to compare with the self-diffusivities measured from PFG NMR (D_{NMR}). The corrected secant diffusivities ($D_{sec,corr}$) showed good alignment with the self-diffusivities, highlighting the robustness of using direct sorption measurements to accurately recover transport diffusivities in systems based on microporous materials.

4.5. Pressure dependence of diffusivity

Pure-gas permeation tests and PFG NMR measurements were performed at varying pressures to investigate the dependence of diffusivities on gas concentration within the membranes. Fig. 5 (a) shows that the permeability decreased with increasing feed pressure, confirming the absence of easily detectable plasticization effects in the tested samples. This decrease in permeability with increasing pressure is anticipated due to the reduction in sorption coefficient at higher pressures based on the dual-mode sorption model. Without significant swelling, the diffusivity should remain relatively constant as pressure increases [54].

Fig. 5 (b) and (c) present the corrected time-lag and secant diffusivities versus feed pressure, respectively. Even after correction for nonideality via Darken's relationship (Eq (15)), the time-lag diffusivities increased with the feed pressure, likely due to the invalid assumption of

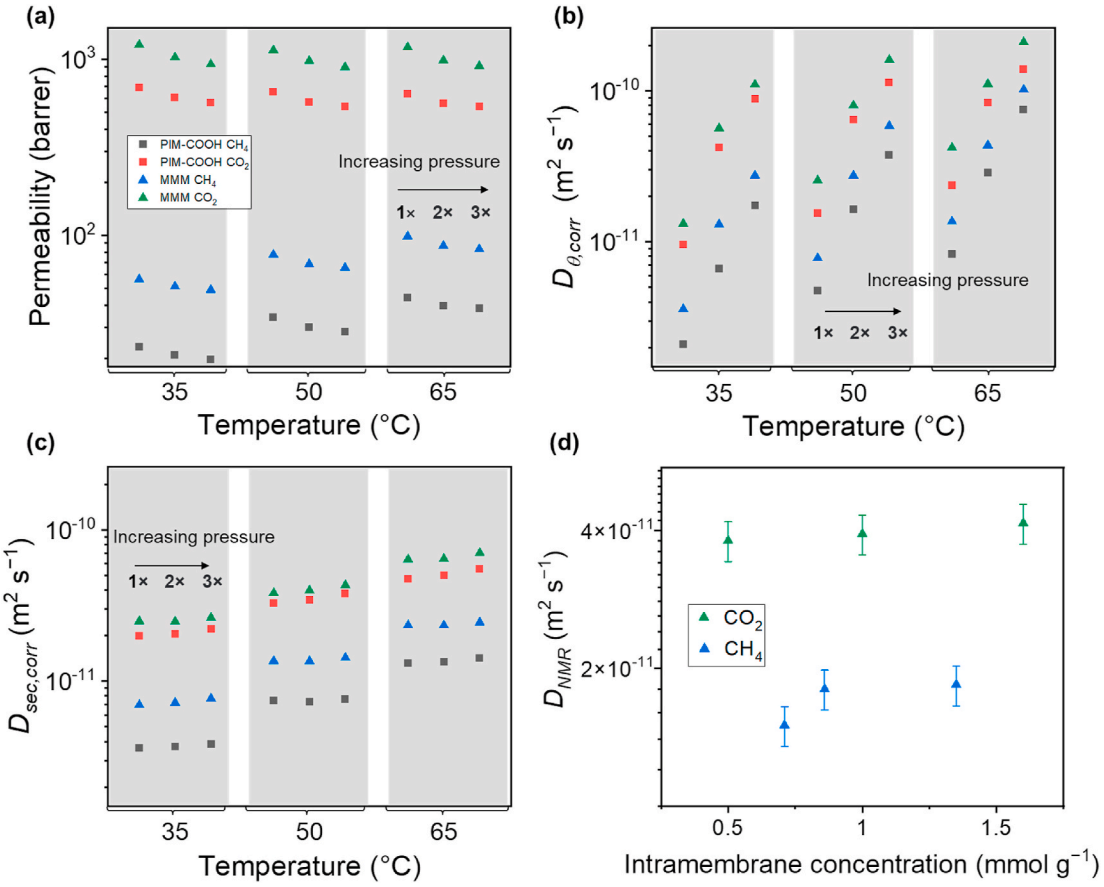

Fig. 5. CH_4 and CO_2 (a) permeability, (b) corrected time-lag diffusivity ($D_{\theta,corr}$), and (c) corrected secant diffusivity ($D_{sec,corr}$) at 35, 50, and 65 °C under increasing feed pressures (1× , 2× , and 3× original feed pressure) in PIM-COOH and a 30 vol% MMM. (d) Self-diffusivities obtained from NMR for a 30 vol% MMM with various CO_2 and CH_4 loadings at 35 °C.

Henry's law sorption behavior in the time-lag method. Paul demonstrated that the time lag decreases with pressure when Eq (1) is applied to glassy polymers, leading to an increase in time-lag diffusivity with pressure [21]. In contrast, the corrected secant diffusivity remained constant over the range of pressures tested, aligning with expectations for samples without structural changes during the permeation test. The pressure dependence of the corrected transient sorption diffusivities ($D_{ts,corr}$) was examined by fitting the CO_2 pressure decay profiles for all the sorption pressure steps at 35 °C for PIM-COOH and MMM. Fig. S7 shows that the fitted $D_{ts,corr}$ generally decreases with increasing pressure. However, the large uncertainties resulting from the fitting prevent definitive conclusions from being drawn about this pressure dependence. Fig. 5 (d) shows that the self-diffusivities of CO_2 and CH_4 in a 30 vol% MMM, as measured via PFG NMR, are independent of intra-membrane concentration in the measured concentration range. This observation aligns with expectations and the trends found for $D_{sec,corr}$. The findings here underscore the importance of using appropriate macroscopic methods to obtain transport diffusivities, as not only the absolute values but also the dependence on other parameters can vary substantially based on model assumptions.

5. Conclusions

This study provided a comprehensive investigation into the microscopic and macroscopic measurements of CH_4 and CO_2 diffusion behaviors in PIM-COOH and a PIM-COOH/UiO-66-NH_2 MMM with 30 vol % MOF loading, using ^{13}C PFG NMR and various macroscopic measurement techniques. PFG NMR results for both pure PIM-COOH films and MMMs revealed mono-exponential and diffusion time-independent attenuation curves that indicate uniform intra-membrane transport properties for length scales comparable with or exceeding the smallest measured RMSD (~1 μm). Macroscopically-measured diffusivities were extracted from permeation tests using the time-lag method and direct sorption analysis. The assumptions used in the time-lag method resulted in systematically lower diffusivities with strong pressure dependence. In contrast, the corrected secant diffusivities showed values comparable to the self-diffusivities obtained from PFG NMR and exhibited minimal pressure dependence, which is expected of non-plasticized membranes. Diffusivities were also obtained from transient sorption experiments, which yielded lower values and higher uncertainties compared to other methods. Overall, this study highlights the strength of PFG NMR in probing microscopic transport directly and underscores the significance of employing the appropriate macroscopic methods to accurately determine diffusivities in microporous material-based MMMs. The insights gained provide valuable information for the future development of advanced materials with improved gas separation properties.

CRediT authorship contribution statement

Wan-Ni Wu: Writing – original draft, Methodology, Investigation, Formal analysis, Data curation, Conceptualization. **Omar Boloki:** Writing – review & editing, Methodology, Investigation, Formal analysis, Data curation, Conceptualization. **Sergey Vasenkov:** Writing – review & editing, Supervision, Conceptualization. **Zachary P. Smith:** Writing – review & editing, Supervision, Conceptualization.

Funding sources

The present work was financially supported by NSF (CBET award No. 2034734, 2034742, and 2146422). A portion of this work was performed in the McKnight Brain Institute at the National High Magnetic Field Laboratory's Advanced Magnetic Resonance Imaging and Spectroscopy (AMRIS) Facility, which is supported by National Science Foundation Cooperative Agreement DMR-1644779, DMR-2128556 and the State of Florida. This work was supported in part by an NIH award, S10 RR031637, for magnetic resonance instrumentation.

Declaration of competing interest

The authors declare that they have no known competing financial interests or personal relationships that could have appeared to influence the work reported in this paper.

Appendix B. Supplementary data

Supplementary data to this article can be found online at https://doi.org/10.1016/j.memsci.2025.124246.

Data availability

Data will be made available on request.

References

[1] L.M. Robeson, Correlation of separation factor versus permeability for polymeric membranes, J. Membr. Sci. 62 (2) (1991) 165–185, https://doi.org/10.1016/0376-7388(91)80060-J.
[2] B. Comesaña-Gándara, J. Chen, C.G. Bezzu, M. Carta, I. Rose, M.C. Ferrari, E. Esposito, A. Fuoco, J.C. Jansen, N.B. McKeown, Redefining the robeson upper bounds for CO_2/CH_4 and CO_2/N_2 separations using a series of ultrapermeable Benzotriptycene-Based polymers of intrinsic microporosity, Energy Environ. Sci. 12 (9) (2019) 2733–2740, https://doi.org/10.1039/c9ee01384a.
[3] Q. Qian, P.A. Asinger, M.J. Lee, G. Han, K. Mizrahi Rodriguez, S. Lin, F. M. Benedetti, A.X. Wu, W.S. Chi, Z.P. Smith, MOF-based membranes for gas separations, Chem. Rev. 120 (16) (2020) 8161–8266, https://doi.org/10.1021/acs.chemrev.0c00119.
[4] F. Dorosti, M. Omidkhah, R. Abedini, Fabrication and characterization of Matrimid/MIL-53 mixed matrix membrane for CO_2/CH_4 separation, Chem. Eng. Res. Des. 92 (11) (2014) 2439–2448, https://doi.org/10.1016/j.cherd.2014.02.018.
[5] R. Adams, C. Carson, J. Ward, R. Tannenbaum, W. Koros, Metal organic framework mixed matrix membranes for gas separations, Microporous Mesoporous Mater. 131 (1–3) (2010) 13–20, https://doi.org/10.1016/j.micromeso.2009.11.035.
[6] J.O. Hsieh, K.J. Balkus, J.P. Ferraris, I.H. Musselman, MIL-53 frameworks in mixed-matrix membranes, Microporous Mesoporous Mater. 196 (2014) 165–174, https://doi.org/10.1016/j.micromeso.2014.05.006.
[7] W.-N. Wu, K. Mizrahi Rodriguez, N. Roy, J.J. Teesdale, G. Han, A. Liu, Z.P. Smith, Engineering the Polymer–MOF interface in microporous composites to address complex mixture separations, ACS Appl. Mater. Interfaces 15 (45) (2023) 52893–52907, https://doi.org/10.1021/acsami.3c11300.
[8] K. Mizrahi Rodriguez, A.X. Wu, Q. Qian, G. Han, S. Lin, F.M. Benedetti, H. Lee, W. S. Chi, C.M. Doherty, Z.P. Smith, Facile and time-efficient carboxylic acid functionalization of PIM-1: effect on molecular packing and gas separation performance, Macromolecules 53 (15) (2020) 6220–6234, https://doi.org/10.1021/acs.macromol.0c00933.
[9] G. Liu, Y. Labreche, V. Chernikova, O. Shekhah, C. Zhang, Y. Belmabkhout, M. Eddaoudi, W.J. Koros, Zeolite-like MOF nanocrystals incorporated 6FDA-Polyimide mixed-matrix membranes for CO_2/CH_4 separation, J. Membr. Sci. 565 (2018) 186–193, https://doi.org/10.1016/j.memsci.2018.08.031.
[10] S. Shahid, K. Nijmeijer, S. Nehache, I. Vankelecom, A. Deratani, D. Quemener, MOF-mixed matrix membranes: precise dispersion of MOF particles with better compatibility via a particle fusion approach for enhanced gas separation properties, J. Membr. Sci. 492 (2015) 21–31, https://doi.org/10.1016/j.memsci.2015.05.015.
[11] M. Lanč, K. Pilnáček, C.R. Mason, P.M. Budd, Y. Rogan, R. Malpass-Evans, M. Carta, B.C. Gándara, N.B. McKeown, J.C. Jansen, O. Vopička, K. Friess, Gas sorption in polymers of intrinsic microporosity: the difference between solubility coefficients determined via time-lag and direct sorption experiments, J. Membr. Sci. 570–571 (2019) 522–536, https://doi.org/10.1016/j.memsci.2018.10.048.
[12] O. Vopička, V. Hynek, M. Zgažar, K. Friess, M. Šípek, A new sorption model with a dynamic correction for the determination of diffusion coefficients, J. Membr. Sci. 330 (1) (2009) 51–56, https://doi.org/10.1016/j.memsci.2008.12.037.
[13] H. Jobic, M. Bée, J. Caro, M. Bülow, J. Kärger, Molecular self-diffusion of methane in zeolite ZSM-5 by quasi-elastic neutron scattering and nuclear magnetic resonance pulsed field gradient technique, J. Chem. Soc. Faraday Trans. 1 Phys. Chem. Condens. Phases 85 (12) (1989) 4201–4209, https://doi.org/10.1039/F19898504201.
[14] O. Boloki, S. Dewitt, E.T. Hahnert, Z.P. Smith, S. Vasenkov, Gas self-diffusion in different local environments of mixed-matrix membranes as a function of UiO-66-NH_2 metal–organic framework loading, Microporous Mesoporous Mater. 378 (2024) 113249, https://doi.org/10.1016/j.micromeso.2024.113249.
[15] K. Díaz, L. Garrido, M. López-González, L.F. del Castillo, E. Riande, CO_2 transport in polysulfone membranes containing zeolitic imidazolate frameworks as determined by permeation and PFG NMR techniques, Macromolecules 43 (1) (2010) 316–325, https://doi.org/10.1021/ma902303e.
[16] A. Baniani, M.P. Rivera, R.P. Lively, S. Vasenkov, Self-diffusion of mixed xylene isomers in ZIF-71 crystals dispersed in a polymer to form a hybrid membrane,

Microporous Mesoporous Mater. 338 (2022) 111960, https://doi.org/10.1016/j.micromeso.2022.111960.
[17] A. Baniani, M.P. Rivera, J. Marreiros, R.P. Lively, S. Vasenkov, Influence of polymer modification on Intra-MOF self-diffusion in MOF-based mixed matrix membranes, Microporous Mesoporous Mater. 359 (2023) 112648, https://doi.org/10.1016/j.micromeso.2023.112648.
[18] W.-N. Wu, Microporous Polymer-Metal Organic Framework (MOF) Hybrid Materials for Separations, Massachusetts Institute of Technology, Thesis, 2024. https://dspace.mit.edu/handle/1721.1/157250. (Accessed 13 April 2025).
[19] R.M. Barrer, E.K. Rideal, Permeation, diffusion and solution of gases in organic polymers, Trans. Faraday Soc. 35 (1939) 628–643, https://doi.org/10.1039/tf9393500628.
[20] J.G. Wijmans, R.W. Baker, The solution–diffusion model: a review, J. Membr. Sci. 107 (1–2) (1995) 1–21, https://doi.org/10.1016/0376-7388(95)00102-I.
[21] D.R. Paul, Gas sorption and transport in glassy polymers, Berichte Bunsenges. Für Phys. Chem. 83 (4) (1979) 294–302, https://doi.org/10.1002/bbpc.19790830403.
[22] G.H. Fredrickson, E. Helfand, Dual-mode transport of penetrants in glassy polymers, Macromolecules 18 (11) (1985) 2201–2207, https://doi.org/10.1021/ma00153a024.
[23] D.R. Paul, W.J. Koros, Effect of partially immobilizing sorption on permeability and the diffusion time lag, J. Polym. Sci. Polym. Phys. Ed. 14 (4) (1976) 675–685, https://doi.org/10.1002/pol.1976.180140409.
[24] H. Odani, T. Uyeda, Theories of sorption and transport in polymer membrane, Polym. J. 23 (5) (1991) 467–479, https://doi.org/10.1295/polymj.23.467.
[25] L. Wang, J.-P. Corriou, C. Castel, E. Favre, Transport of gases in glassy polymers under transient conditions: limit-behavior investigations of dual-mode sorption theory, Ind. Eng. Chem. Res. 52 (3) (2013) 1089–1101, https://doi.org/10.1021/ie2027102.
[26] O. Vopička, K. Friess, V. Hynek, P. Sysel, M. Zgažar, M. Šípek, K. Pilnáček, M. Lanč, J.C. Jansen, C.R. Mason, P.M. Budd, Equilibrium and transient sorption of vapours and gases in the polymer of intrinsic microporosity PIM-1, J. Membr. Sci. 434 (2013) 148–160, https://doi.org/10.1016/j.memsci.2013.01.040.
[27] J. Crank, The Mathematics of Diffusion, Clarendon Press, 1979.
[28] H. Jobic, J. Kärger, M. Bée, Simultaneous measurement of Self- and transport diffusivities in zeolites, Phys. Rev. Lett. 82 (21) (1999) 4260–4263, https://doi.org/10.1103/PhysRevLett.82.4260.
[29] R. Mueller, R. Kanungo, M. Kiyono-Shimobe, W.J. Koros, S. Vasenkov, Diffusion of methane and carbon dioxide in carbon molecular sieve membranes by multinuclear pulsed field gradient NMR, Langmuir 28 (27) (2012) 10296–10303, https://doi.org/10.1021/la301674k.
[30] J. Karger, D.M. Ruthven, On the comparison between macroscopic and n.m.r. measurements of intracrystalline diffusion in zeolites, Zeolites 9 (4) (1989) 267–281, https://doi.org/10.1016/0144-2449(89)90071-7.
[31] G.C. Shearer, J.G. Vitillo, S. Bordiga, S. Svelle, U. Olsbye, K.P. Lillerud, Functionalizing the defects: postsynthetic ligand exchange in the metal organic framework UiO-66, Chem. Mater. 28 (20) (2016) 7190–7193, https://doi.org/10.1021/acs.chemmater.6b02749.
[32] J. Rouquerol, P.L. Llewellyn, J. Rouquerol, P. Llewellyn, F. Rouquerol, Characterization of porous, Solids VII 160 (2007) 49–56, https://doi.org/10.1016/S0167-2991(07)80008-5.
[33] T. Düren, F. Millange, G. Férey, K.S. Walton, R.Q. Snurr, Calculating geometric surface areas as a characterization tool for metal-organic frameworks, J. Phys. Chem. C 111 (42) (2007) 15350–15356, https://doi.org/10.1021/jp074723h.
[34] J.W.M. Osterrieth, J. Rampersad, D. Madden, N. Rampal, L. Skoric, B. Connolly, M. D. Allendorf, V. Stavila, J.L. Snider, R. Ameloot, J. Marreiros, C. Ania, D. Azevedo, E. Vilarrasa-Garcia, B.F. Santos, X.H. Bu, Z. Chang, H. Bunzen, N.R. Champness, S. L. Griffin, B. Chen, R.B. Lin, B. Coasne, S. Cohen, J.C. Moreton, Y.J. Colón, L. Chen, R. Clowes, F.X. Coudert, Y. Cui, B. Hou, D.M. D'Alessandro, P.W. Doheny, M. Dincă, C. Sun, C. Doonan, M.T. Huxley, J.D. Evans, P. Falcaro, R. Ricco, O. Farha, K.B. Idrees, T. Islamoglu, P. Feng, H. Yang, R.S. Forgan, D. Bara, S. Furukawa, E. Sanchez, J. Gascon, S. Telalović, S.K. Ghosh, S. Mukherjee, M. R. Hill, M.M. Sadiq, P. Horcajada, P. Salcedo-Abraira, K. Kaneko, R. Kukobat, J. Kenvin, S. Keskin, S. Kitagawa, K. ichi Otake, R.P. Lively, S.J.A. DeWitt, P. Llewellyn, B.V. Lotsch, S.T. Emmerling, A.M. Pütz, C. Martí-Gastaldo, N. M. Padial, J. García-Martínez, N. Linares, D. Maspoch, J.A. Suárez del Pino, P. Moghadam, R. Oktavian, R.E. Morris, P.S. Wheatley, J. Navarro, C. Petit, D. Danaci, M.J. Rosseinsky, A.P. Katsoulidis, M. Schröder, X. Han, S. Yang, C. Serre, G. Mouchaham, D.S. Sholl, R. Thyagarajan, D. Siderius, R.Q. Snurr, R. B. Goncalves, S. Telfer, S.J. Lee, V.P. Ting, J.L. Rowlandson, T. Uemura, T. Iiyuka, M.A. van der Veen, D. Rega, V. Van Speybroeck, S.M.J. Rogge, A. Lamaire, K. S. Walton, L.W. Bingel, S. Wuttke, J. Andreo, O. Yaghi, B. Zhang, C.T. Yavuz, T. S. Nguyen, F. Zamora, C. Montoro, H. Zhou, A. Kirchon, D. Fairen-Jimenez, How reproducible are surface areas calculated from the BET equation? Adv. Mater. 34 (27) (2022) 2201502 https://doi.org/10.1002/adma.202201502.
[35] G. Han, K.M. Rodriguez, Q. Qian, Z.P. Smith, Acid-modulated synthesis of high surface area amine-functionalized MIL-101(Cr) nanoparticles for CO_2 separations, Ind. Eng. Chem. Res. 59 (40) (2020) 18139–18150, https://doi.org/10.1021/acs.iecr.0c03456.
[36] Y. Lin, C. Kong, L. Chen, Direct synthesis of amine-functionalized MIL-101(Cr) nanoparticles and application for CO_2 capture, RSC Adv. 2 (16) (2012) 6417–6419, https://doi.org/10.1039/c2ra20641b.
[37] K. Mizrahi Rodriguez, S. Lin, A.X. Wu, G. Han, J.J. Teesdale, C.M. Doherty, Z. P. Smith, Leveraging free volume manipulation to improve the membrane separation performance of amine-functionalized PIM-1, Angew. Chem. 133 (12) (2021) 6667–6673, https://doi.org/10.1002/ange.202012441.
[38] K. Mizrahi Rodriguez, F.M. Benedetti, N. Roy, A.X. Wu, Z.P. Smith, Sorption-enhanced mixed-gas transport in amine functionalized polymers of intrinsic microporosity (PIMs), J. Mater. Chem. A 9 (41) (2021) 23631–23642, https://doi.org/10.1039/d1ta06530k.
[39] K. Mizrahi Rodriguez, W.N. Wu, T. Alebrahim, Y. Cao, B.D. Freeman, D. Harrigan, M. Jhalaria, A. Kratochvil, S. Kumar, W.H. Lee, Y.M. Lee, H. Lin, J.M. Richardson, Q. Song, B. Sundell, R. Thür, I. Vankelecom, A. Wang, L. Wang, C. Wiscount, Z. P. Smith, Multi-lab study on the pure-gas permeation of commercial polysulfone (PSf) membranes: measurement standards and best practices, J. Membr. Sci. 659 (2022) 120746, https://doi.org/10.1016/j.memsci.2022.120746.
[40] R.S. Bhavsar, T. Mitra, D.J. Adams, A.I. Cooper, P.M. Budd, Ultrahigh-permeance PIM-1 based thin film nanocomposite membranes on PAN supports for CO_2 separation, J. Membr. Sci. 564 (2018) 878–886, https://doi.org/10.1016/j.memsci.2018.07.089.
[41] S.J.D. Smith, B.P. Ladewig, A.J. Hill, C.H. Lau, M.R. Hill, Post-synthetic Ti exchanged UiO-66 metal-organic frameworks that deliver exceptional gas permeability in mixed matrix membranes, Sci. Rep. 5 (1) (2015) 7823, https://doi.org/10.1038/srep07823.
[42] M. Dvoyashkin, J. Zang, G.I. Yucelen, A. Katihar, S. Nair, D.S. Sholl, C.R. Bowers, S. Vasenkov, Diffusion of tetrafluoromethane in single-walled aluminosilicate nanotubes: pulsed field gradient NMR and molecular dynamics simulations, J. Phys. Chem. C 116 (40) (2012) 21350–21355, https://doi.org/10.1021/jp3054247.
[43] R. Mueller, S. Zhang, C. Zhang, R. Lively, S. Vasenkov, Relationship between long-range diffusion and diffusion in the ZIF-8 and polymer phases of a mixed-matrix membrane by high field NMR diffusometry, J. Membr. Sci. 477 (2015) 123–130, https://doi.org/10.1016/j.memsci.2014.12.015.
[44] R. Span, W. Wagner, A new equation of state for carbon dioxide covering the fluid region from the triple-point temperature to 1100 K at pressures up to 800 MPa, J. Phys. Chem. Ref. Data 25 (6) (1996) 1509–1596, https://doi.org/10.1063/1.555991.
[45] U. Setzmann, W. Wagner, A new equation of state and tables of thermodynamic properties for methane covering the range from the melting line to 625 K at pressures up to 1000 MPa, J. Phys. Chem. Ref. Data 20 (6) (1991) 1061–1155, https://doi.org/10.1063/1.555898.
[46] R.M. Cotts, M.J.R. Hoch, T. Sun, J.T. Markert, Pulsed field gradient stimulated echo methods for improved NMR diffusion measurements in heterogeneous systems, J. Magn. Reson. 83 (2) (1989) 252–266, https://doi.org/10.1016/0022-2364(89)90189-3, 1969.
[47] S.J. Gibbs, C.S. Johnson, A PFG NMR experiment for accurate diffusion and flow studies in the presence of eddy currents, J. Magn. Reson. 93 (2) (1991) 395–402, https://doi.org/10.1016/0022-2364(91)90014-K, 1969.
[48] J. Kärger, D. Ruthven, D. Theodorou, Diffusion measurement by monitoring molecular displacement, in: Diffusion in Nanoporous Materials, John Wiley & Sons, Ltd, 2012, pp. 347–394, https://doi.org/10.1002/9783527651276.ch11.
[49] M.Z. Ahmad, M. Navarro, M. Lhotka, B. Zornoza, C. Téllez, W.M. de Vos, N. E. Benes, N.M. Konnertz, T. Visser, R. Semino, G. Maurin, V. Fila, J. Coronas, Enhanced gas separation performance of 6FDA-DAM based mixed matrix membranes by incorporating MOF UiO-66 and its derivatives, J. Membr. Sci. 558 (2018) 64–77, https://doi.org/10.1016/j.memsci.2018.04.040.
[50] B.W. Rowe, L.M. Robeson, B.D. Freeman, D.R. Paul, Influence of temperature on the upper bound: theoretical considerations and comparison with experimental results, J. Membr. Sci. 360 (1) (2010) 58–69, https://doi.org/10.1016/j.memsci.2010.04.047.
[51] Y. Liu, G. Liu, C. Zhang, W. Qiu, S. Yi, V. Chernikova, Z. Chen, Y. Belmabkhout, O. Shekhah, M. Eddaoudi, W. Koros, Enhanced CO_2/CH_4 separation performance of a mixed matrix membrane based on tailored MOF-polymer formulations, Adv. Sci. 5 (9) (2018) 1800982, https://doi.org/10.1002/advs.201800982.
[52] L.M. Robeson, The upper bound revisited, J. Membr. Sci. 320 (1–2) (2008) 390–400, https://doi.org/10.1016/j.memsci.2008.04.030.
[53] M.H. Klopffer, B. Flaconneche, Transport properties of gases in polymers: bibliographic review, Oil Gas Sci. Technol. 56 (3) (2001) 223–244, https://doi.org/10.2516/ogst:2001021.
[54] K.M. Rodriguez, S. Lin, A.X. Wu, K.R. Storme, T. Joo, A.F. Grosz, N. Roy, D. Syar, F. M. Benedetti, Z.P. Smith, Penetrant-induced plasticization in microporous polymer membranes, Chem. Soc. Rev. 53 (2024) 2435–2529, https://doi.org/10.1039/d3cs00235g.